OPEN ACCESS



X-Ray Spectroscopy in the Microcalorimeter Era 4: Optical Depth Effects on the Soft X-Rays Studied with CLOUDY

Priyanka Chakraborty^{1,2}, Gary J. Ferland², Marios Chatzikos², Andrew C. Fabian³, Stefano Bianchi⁴, Francisco Guzmán⁵, and Yuanyuan Su², and Yuanyuan Su

Abstract

In this paper, we discuss atomic processes modifying the soft X-ray spectra from optical depth effects like photoelectric absorption and electron scattering suppressing the soft X-ray lines. We also show the enhancement in soft X-ray line intensities in a photoionized environment via continuum pumping. We quantify the suppression/enhancement by introducing a "line modification factor ($f_{\rm mod}$)." If $0 \leqslant f_{\rm mod} \leqslant 1$, the line is suppressed, which could be the case in both collisionally ionized and photoionized systems. If $f_{\rm mod} \geqslant 1$, the line is enhanced, which occurs in photoionized systems. Hybrid astrophysical sources are also very common, where the environment is partly photoionized and partly collisionally ionized. Such a system is V1223 Sgr, an Intermediate Polar binary. We show the application of our theory by fitting the first-order Chandra Medium Energy Grating (MEG) spectrum of V1223 Sgr with a combination of CLOUDY-simulated additive cooling-flow and photoionized models. In particular, we account for the excess flux for O VII, O VIII, Ne IX, Ne X, and Mg XI lines in the spectrum found in a recent study, which could not be explained with an absorbed cooling-flow model.

Unified Astronomy Thesaurus concepts: X-ray binary stars (1811); Atomic spectroscopy (2099)

1. Introduction

The strongest emission lines observed in the soft X-ray spectra of astrophysical plasmas are H-like and He-like lines from elements between carbon and sulfur, and Fe L-shell lines. Such X-ray emitting plasmas can be collisionally ionized or photoionized. In collisionally ionized plasma, ionization or excitation events mainly occur due to electron—ion collisions. In photoionized plasma, ionization is dominated by the interaction between photons and ions/atoms. A hybrid of the two types of plasma is also possible, where the cloud is partly collisionally ionized and partly photoionized.

Line intensity in observed X-ray spectra can be enhanced or suppressed depending on the following factors. If photoionized, lines may be (a) enhanced when electrons bound to the ions absorb photons of appropriate wavelength transitioning to higher energy states followed by radiative cascades, also known as continuum pumping, or (b) suppressed due to optical depth effects. If collisionally ionized, only optical depth effects suppress lines in the X-ray spectra. In the soft X-ray regime, the optical depth effects leading to line suppression mainly come from photoelectric absorption of line photons or scattering by electrons. Sections 2 and 3 present more detailed discussion.

The effects of continuum pumping on the optically thin line intensities, the so-called "Case C," was introduced by Baker et al. (1938) and later discussed by Chamberlain (1953) and Ferland (1999). Their study was later extended to describe "Case D" (Luridiana et al. 2009; Peimbert et al. 2016), the optically thick counterpart of Case C. Recently, Chakraborty et al. (2021)

Original content from this work may be used under the terms of the Creative Commons Attribution 4.0 licence. Any further distribution of this work must maintain attribution to the author(s) and the title of the work, journal citation and DOI.

discussed Case C and Case D in view of the future microcalorimeter missions line XRISM and Athena, focusing on line emission from H- and He-like iron.

Optical depth effects on soft X-ray spectra have been previously investigated by Storey & Hummer (1988) and Hummer & Storey (1992), who calculated the recombination line intensities of H-like carbon, nitrogen, and oxygen assuming "Case B" (Baker & Menzel 1938) and discussed the effects of finite optical depth and dust on H-like ions. Such effects have also been observed in soft X-ray emission spectra. For instance, recent analysis of soft X-ray spectra from the Reflection Grating Spectrometer on board XMM-Newton and the High Energy Transmission Grating Spectrometer on board Chandra explored several optically thick astrophysical sources like cataclysmic variables (CVs), novae, ultraluminous X-ray sources, Seyfert galaxies, elliptical galaxies, X-ray binaries, etc. (Ramsay & Cropper 2002; Rauch et al. 2005; Okada et al. 2008; Pintore & Zampieri 2011; de Plaa et al. 2012; Matzeu et al. 2020; Amato et al. 2021).

As previously mentioned, there have been extensive studies separately discussing the effects of continuum pumping and optical depth effects on X-ray line intensities. The current need is to develop a comprehensive theory that will account for all the atomic processes changing the soft X-ray spectra. This paper aims to present a framework for interpreting the soft X-ray spectra from photoionized and collisionally ionized plasma using the spectral synthesis code CLOUDY (Ferland et al. 2017). A cooling-flow model has been introduced to treat the multiphase collisionally ionized systems.

We also show the application of our model on V1223 Sgr, a member of the cataclysmic variable binary star systems called Intermediate Polars (IPs). We address the lack of emission from several lower atomic number H- and He-like ions, as mentioned

in Islam & Mukai (2021), with additive cooling-flow and photoionized models. However, our model will be applicable for any optically thick⁶ source with/without a radiation source.

This paper is the fourth of the series "X-ray spectroscopy in the microcalorimeter era." The first three papers discussed the atomic processes in a collisionally excited and photoionized astrophysical plasma for H- and He-like iron for a wide range of column densities. Chakraborty et al. (2020a) explored the effects of Li-like iron on the line intensities of four members of the Fe XXV K α complex—x($2^3P_2 \rightarrow 1^1S$), y($2^3P_1 \rightarrow 1^1S$), z($2^3S \rightarrow 1^1S$), and w($2^1P \rightarrow 1^1S$) through resonant Auger destruction (RAD; Ross et al. 1978; Band et al. 1990; Ross et al. 1996; Liedahl 2005) and line broadening effects by electron scattering. Chakraborty et al. (2020b) introduced a novel method of measuring column density from Case A to B (optically thin to thick) transition by comparing the observed spectra by Hitomi with spectra simulated with CLOUDY. Chakraborty et al. (2021) established four asymptotic limits, Cases A, B, C, and D, for describing the line formation processes in H- and He-like iron emitting in the X-rays. This paper is a continuation of the framework discussed in the first three papers to study the atomic processes affecting the soft X-ray spectrum.

2. Line Suppression Due to Photoelectric and Electron Opacity

Photoelectric absorption of line photons or scattering by electrons can significantly suppress line intensities. Here we present CLOUDY calculations of the net emission, demonstrate line suppression due to absorption and scattering, and give simple analytical estimates of the physical processes that suppress the line emission.

CLOUDY actually determines the line emission by solving a fully coupled system of equations giving radiative transitions between levels, as originally described in Section III of Rees et al. (1989). The numerical results can be understood by considering the following approximations to the line transfer.

The fraction of photons that survives (which we call f_{mod} or the "line modification factor") after N scatterings that is subject to photoelectric absorption and electron scattering is determined by the following equation:

$$f_{\text{mod}} = (1 - P_{\text{photoelectric}} - P_{\text{scattering}})^N,$$
 (1)

where N is the mean number of scatterings experienced by a line photon with a line-center optical depth τ before escaping an optically thick cloud (Ferland & Netzer 1979):

$$N = \frac{1.11\tau^{1.071}}{1 + (\log \tau / 5.5)^5}.$$
 (2)

 $P_{\rm photoelectric}$ is the probability of photoelectric absorption per scattering, and is given by the following ratio of opacities:

$$P_{\text{photoelectric}} = \frac{\kappa_{\text{photoelectric}}}{\kappa_{\text{total}}}.$$
 (3)

 $P_{\text{scattering}}$ is the probability per scattering that a line photon will be scattered off free electrons due to the very large Doppler shift they receive and be removed from the Doppler core of the

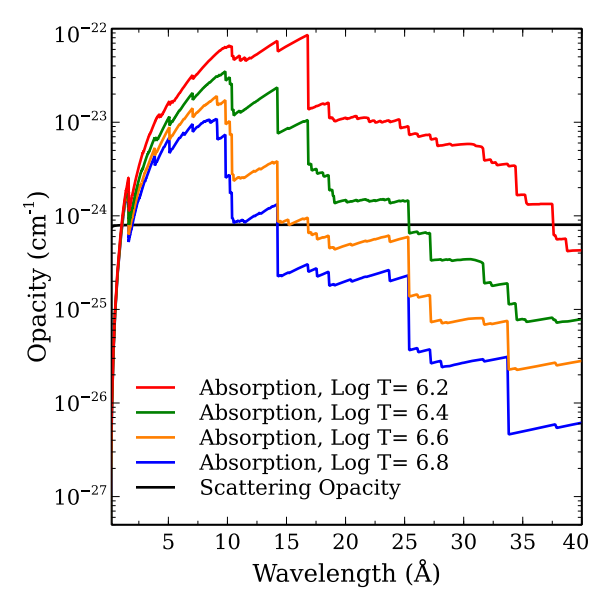


Figure 1. Continuum opacities plotted as a function of wavelength for a cloud with $N_{\rm H}=10^{23}\,{\rm cm}^{-2}$. Red, green, yellow, and blue solid lines show the absorption opacities (photoelectric) for log $T=6.2,~6.4,~6.6,~{\rm and}~6.8,$ respectively. The black solid line shows the electron scattering opacity. The opacity is in units of per centimeter; the unit of opacity appearing in Kirchhoff–Planck law is per centimeter.

line (refer to Section 7.1 in Chakraborty et al. 2020a for a detailed discussion):

$$P_{scattering} = \frac{\kappa_{scattering}}{\kappa_{total}},\tag{4}$$

where the total opacity is given by

$$\kappa_{\text{total}} = \kappa_{\text{line}} + \kappa_{\text{photoelectric}} + \kappa_{\text{scattering}}.$$
(5)

For the most part, $f_{\rm mod}$ gives an estimate for the fraction of photons surviving after photoelectric absorption and electron scattering. Figure 1 shows photoelectric absorption opacities ($\kappa_{\rm photoelectric}$) for temperatures between $\log T({\rm Kelvin}) = 6.2$ and $\log T({\rm Kelvin}) = 6.8$ and the electron scattering opacity ($\kappa_{\rm scattering}$), assuming a thermal collisional equilibrium at T. A hydrogen density ($n({\rm H})$) of 1 cm⁻³ was assumed, corresponding to an electron density of ~ 1.2 cm⁻³, hydrogen and helium being the two most abundant elements in the universe. The electron scattering opacity was evaluated by multiplying the electron scattering cross section (6.65×10^{-25} cm²) with its density. Scattering is more important at the longer wavelengths and higher temperatures, while absorption is more important at the shorter wavelengths and lower temperatures. Electron scattering opacity has been estimated.

Other optical depth effects such as the Case A to B transition and RAD can suppress/amplify selected line intensities too (Chakraborty et al. 2020a, 2020b). Numerical CLOUDY simulations on optical depth effects shown in this paper include all the atomic processes that can change line intensities. However, we found these effects insignificant compared to photoelectric absorption and electron scattering in the soft X-ray regime. The discussion on the optical depth effects on soft X-ray emission continues in Section 4 for the collisionally ionized and photoionized cases.

Note that Equation (1) applies in collisionally ionized environments, where there is no external radiation source. In irradiated photoionized environments, $f_{\rm mod}$ will also have contributions from radiative cascades prompted by absorption

⁶ Note that Cloudy generates a warning when the electron scattering optical depth is greater than 5 (refer to cloudy/source/prt_comment.cpp : 2297), corresponding to a hydrogen column density of $7.5 \times 10^{24} \, \mathrm{cm}^{-2}$. All our simulations are done for $N_{\rm H} \le 7.5 \times 10^{24} \, \mathrm{cm}^{-2}$.

of line photons from the external radiation source, also known as "continuum pumping." This is further elaborated in Sections 3 and 4.2.

3. Line Enhancement Due to Continuum Pumping

In photoionized systems, emission lines are enhanced in the presence of external radiation fields due to continuum pumping. Chakraborty et al. (2021) discussed the concept of continuum pumping and its effects in enhancing the line emission from H- and He-like iron. Lines can be enhanced up to $\sim\!30$ times, and the degree of enhancement decreases with the increase in column density due to the optical depth effects, the so-called Case C to D transition. Refer to Section 2 in their paper for the mathematical framework of continuum pumping and Figure 1 for a simplified three level representation of Case C and Case D.

This work is an extension of the same concept for the soft X-ray regime. The observed spectra (photoionized) will have contributions from line enhancement due to continuum pumping and line suppression due to photoelectric absorption and electron scattering (further discussed in Section 4). Whether the lines are enhanced or suppressed depends on the interplay between these effects. The enhancement/suppression varies with the column density/optical depth, ionization parameter (ξ), and shape of the incident radiation field. For most of our calculations, we assume a power-law spectral energy distribution (SED):

$$f_{\nu} \propto \nu^{\alpha}$$
 (6)

with $\alpha = -1$, except for Section 5 where we let α to vary freely.

4. Optical Depth Effects on Soft X-ray Spectra

4.1. Collisionally Ionized Emission Lines

The practical way to study the effect of optical depth on line intensities is to compute scaled line intensity ratios of a realistic model that includes all the optical depth effects and a simplistic model excluding optical depth effects. The line ratio stands for what fraction of line photons survive.

The realistic model includes absorption and scattering. By default, CLOUDY models include absorption but do not include scattering. At X-ray temperatures, a fraction of the line photons gets largely Doppler-shifted from their line center due to scattering off high-speed electrons. The following CLOUDY command reports the line intensities excluding these Doppler-shifted photons:

no scattering intensity.

Refer to Section 6 of Chakraborty et al. (2021) for a detailed discussion on no scattering intensity.

In the simplistic model, absorption was switched off with the command:

no absorption escape.

The smaller the ratio between the realistic and simplistic model, the larger the suppression. This ratio is the numerical equivalent of $f_{\rm mod}$, the line modification factor, studied in Section 2, which presented an analytical discussion on line suppression in optically thick clouds. Figure 2 shows this ratio for selected soft X-ray lines evaluated with CLOUDY.

Temperature and column density are physical parameters that can notably change line emission from the collisionally ionized cloud. Thus, contour plots have been shown where temperature and column density is varied. Metallicity has been fixed at solar for simplicity. In principle, metallicity should not be taken as a free parameter, as optical depth is proportional to metallicity. This section aims to establish the framework using simplified parameters. In Section 5, we let metallicity vary as a free parameter along with other physical parameters to fit the observed spectrum from V1223 Sgr.

Four panels in the figure show the numerical line modification factor for C VI Ly α ($\lambda = 33.736$ Å), O VII K α resonance line (w; $\lambda = 21.602$ Å), O VIII Ly α ($\lambda = 18.969$ Å), and Fe XVII ($\lambda = 15.015$ Å) as a function of the hydrogen column density and temperature for a hydrogen density (n(H)) of 1 cm⁻³. There is significant suppression in carbon and oxygen lines and moderate suppression in the iron lines. For example, for C VI Ly α line at the temperature of its peak emissivity, log T = 6.2; at $N_{\rm H} = 10^{23}$ cm⁻², the numerical line modification factor as shown in the top-left panel of the figure is ~ 0.15 . This implies, only 15 % of the C VI Ly α line photons will make it out of the optically thick cloud at the mentioned temperature and column density.⁷

Numerical results in the figure account for the full physics and the variation of the physical conditions across the cloud. Analytically, Equation (1) estimates the fraction of C VI Ly α photons surviving after photoelectric absorption and electron scattering, the only two important sources of opacity in the soft X-ray limit.

At the same temperature and column density, $\tau \sim 500$ (calculated using the CLOUDY command save line optical depth), $\kappa_{\rm photoelectric} = 3.5 \times 10^{-24} \, {\rm cm}^{-1}$, and $\kappa_{\rm scattering} = 7.9 \times 10^{-25} \, {\rm cm}^{-1}$ (refer to Figure 1). Line opacity ($\kappa_{\rm line}$) can be expressed as a product of ionic number density ($n_{\rm ion}$), and absorption cross section (α_{ν}) for the corresponding transition:

$$\kappa_{\rm line} = n_{\rm ion} \alpha_{\nu}.$$
(7)

Here

$$n_{\rm ion} = {\rm carbon\ abundance}$$

 $\times {\rm ionic\ fraction\ of\ } {\rm C}^{5+} \times {\rm n(H)},$ (8)

and α_{ν} is described by the following equation (see Equation (5.23) in hazy2):

$$\alpha_{\nu(x)} = 2.24484 \times 10^{-14} A_{u,l} \lambda_{\mu m}^3 \frac{g_u}{g_l} \frac{\varphi_{\nu}(x)}{u_{\text{Dop}}}.$$
 (9)

 $A_{u,l}$ is the transition probability for the transition from level u to level 1, $\lambda_{\mu m}$ is the wavelength in micrometer, g_u and g_l are statistical weights of levels u and 1, u_{Dop} is the Doppler velocity, and $\varphi_{\nu}(x)=1$ at the line center. At log T=6.2, $u_{Dop}=\sqrt{\frac{2kT}{m_C}}\sim 47~{\rm km\,s^{-1}}$. Using Equations (7), (8), and (9), we obtain $\kappa_{\rm line}=2.39\times 10^{-21}~{\rm cm^{-1}}$, which implies $\kappa_{\rm total}=2.40\times 10^{-21}~{\rm cm^{-1}}$, and $f_{\rm mod}\sim 0.2$. Analytically, 20% of the C VI Ly α line photons will survive and make it out of the cloud.

Tables 1 and 2 list the numerical value of $f_{\rm mod}$ at $N_{\rm H}=10^{22}\,{\rm cm^{-2}}$, $N_{\rm H}=10^{22.5}\,{\rm cm^{-2}}$, and $N_{\rm H}=10^{23}\,{\rm cm^{-2}}$ for log T=6.4, and 6.8 for important lines in soft X-ray spectra. The listed $f_{\rm mod}$ values are shown as example cases to demonstrate the effect of line modification for a range of astrophysical plasma. The users can generate $f_{\rm mod}$ for the full

We predict the line mean intensity $4\pi J$ averaged over all directions.

Table 1
Line Modification Factor (f_{mod}) in Collisionally Ionized Cloud at $N_{\text{H}} = 10^{22} \text{ cm}^{-2}$, $N_{\text{H}} = 10^{22.5} \text{ cm}^{-2}$, and $N_{\text{H}} = 10^{23} \text{ cm}^{-2}$ and $\log T = 6.4$ for Important Lines in Soft X-Ray Spectra

Transitions	λ (Å)	Label	$f_{ m mod}$			
			$N_{\rm H} = 10^{22} {\rm cm}^{-2}$	$N_{\rm H} = 10^{22.5} {\rm cm}^{-2}$	$N_{\rm H} = 10^{23} {\rm cm}^{-2}$	
C VI	33.736	Ly α	0.57	0.43	0.20	
N VI	29.082	$K\alpha$ (x)	0.40	0.21	0.05	
N VI	28.787	$K\alpha$ (w)	0.37	0.18	0.04	
N VII	24.781	$Ly\alpha$	0.83	0.69	0.24	
O VII	22.101	$K\alpha$ (z)	0.73	0.35	0.13	
O VII	21.807	$K\alpha$ (y)	0.71	0.33	0.12	
O VII	21.804	$K\alpha$ (x)	0.68	0.31	0.11	
O VII	21.602	$K\alpha$ (w)	0.61	0.24	0.08	
O VIII	18.969	$Ly\alpha$	0.82	0.58	0.35	
Fe XVII	15.262	3D ^a	0.84	0.61	0.40	
Fe XVII	15.015	3C ^a	0.86	0.62	0.46	
Ne IX	13.699	$K\alpha$ (z)	0.99	0.97	0.65	
Ne IX	13.553	$K\alpha$ (y)	0.99	0.95	0.61	
Ne IX	13.550	$K\alpha(x)$	0.96	0.87	0.53	
Ne IX	13.447	$K\alpha$ (w)	0.81	0.64	0.33	

Note. Lines from lower atomic number elements are more suppressed than those of higher atomic number elements, as mentioned in Section 4.1.

Table 2
Line Modification Factor ($f_{\rm mod}$) in Collisionally Ionized Cloud at $N_{\rm H}=10^{22}~{\rm cm}^{-2}$, $N_{\rm H}=10^{22.5}~{\rm cm}^{-2}$, and $N_{\rm H}=10^{23}~{\rm cm}^{-2}$ and $\log~T=6.8$ for Important Lines in Soft X-Ray Spectra

			$f_{ m mod}$		
Transitions	λ (Å)	Label	$N_{\rm H} = 10^{22} {\rm cm}^{-2}$	$N_{\rm H} = 10^{22.5} {\rm cm}^{-2}$	$N_{\rm H} = 10^{23} {\rm cm}^{-2}$
O VIII	18.969	$Ly\alpha$	0.89	0.72	0.43
Fe XVII	17.096	M2 ^a	1.0	0.99	0.97
Fe XVII	17.051	3G ^a	1.0	1.0	1.0
Fe XVII	15.262	3D ^a	0.88	0.71	0.50
Fe XVII	15.015	3C ^a	0.91	0.81	0.64
Ne IX	13.699	$K\alpha$ (z)	0.95	0.88	0.74
Ne IX	13.553	$K\alpha$ (y)	0.95	0.87	0.72
Ne IX	13.550	$K\alpha$ (x)	0.94	0.85	0.69
Ne IX	13.447	$K\alpha$ (w)	0.93	0.82	0.62
Ne X	12.134	$Ly\alpha$	0.95	0.86	0.69
Mg XI	9.314	$K\alpha$ (z)	0.99	0.97	0.92
Mg XI	9.231	$K\alpha$ (y)	0.99	0.96	0.90
Mg XI	9.228	$K\alpha(x)$	0.97	0.93	0.84
Mg XI	9.169	$K\alpha$ (w)	0.95	0.85	0.71
Mg XII	8.421	$Ly\alpha$	1.0	1.0	0.98
Si XIII	6.740	$K\alpha$ (z)	1.0	1.0	1.0
Si XIII	6.688	$K\alpha$ (y)	1.0	1.0	1.0
Si XIII	6.685	$K\alpha(x)$	1.0	1.0	1.0
Si XIII	6.648	$K\alpha$ (w)	0.97	0.90	0.80
S XV	5.102	$K\alpha$ (z)	1.0	1.0	1.0
S xv	5.066	K α (y)	1.0	1.0	1.0
S xv	5.063	$K\alpha(x)$	1.0	1.0	1.0
S XV	5.039	$K\alpha$ (w)	1.0	1.0	0.96

Note. Suppression is less than that listed in Table 1 as photoelectric absorption decreases with an increase in temperature. Lines from lower atomic number elements are more suppressed.

parameter space shown in Figure 2 using the CLOUDY command

save line intensity,

along with the CLOUDY commands described earlier in Section 4.1. $f_{\rm mod}$ gives the fraction of line photons that will be observed by high-resolution telescopes. Note that the emission lines from the lower-Z elements exhibit maximum emissivity at the lower temperatures, where the photoelectric absorption is

significant (see Figure 1). This will lead to a larger suppression in the lines from lower-Z elements than those of the higher-Z elements.

4.2. Photoionized Emission Lines

Photoionized emission lines can be enhanced or suppressed, which is determined by the following two factors. (a) All

^a Labeled by Brown et al. (1998).

^a Labeled by Brown et al. (1998).

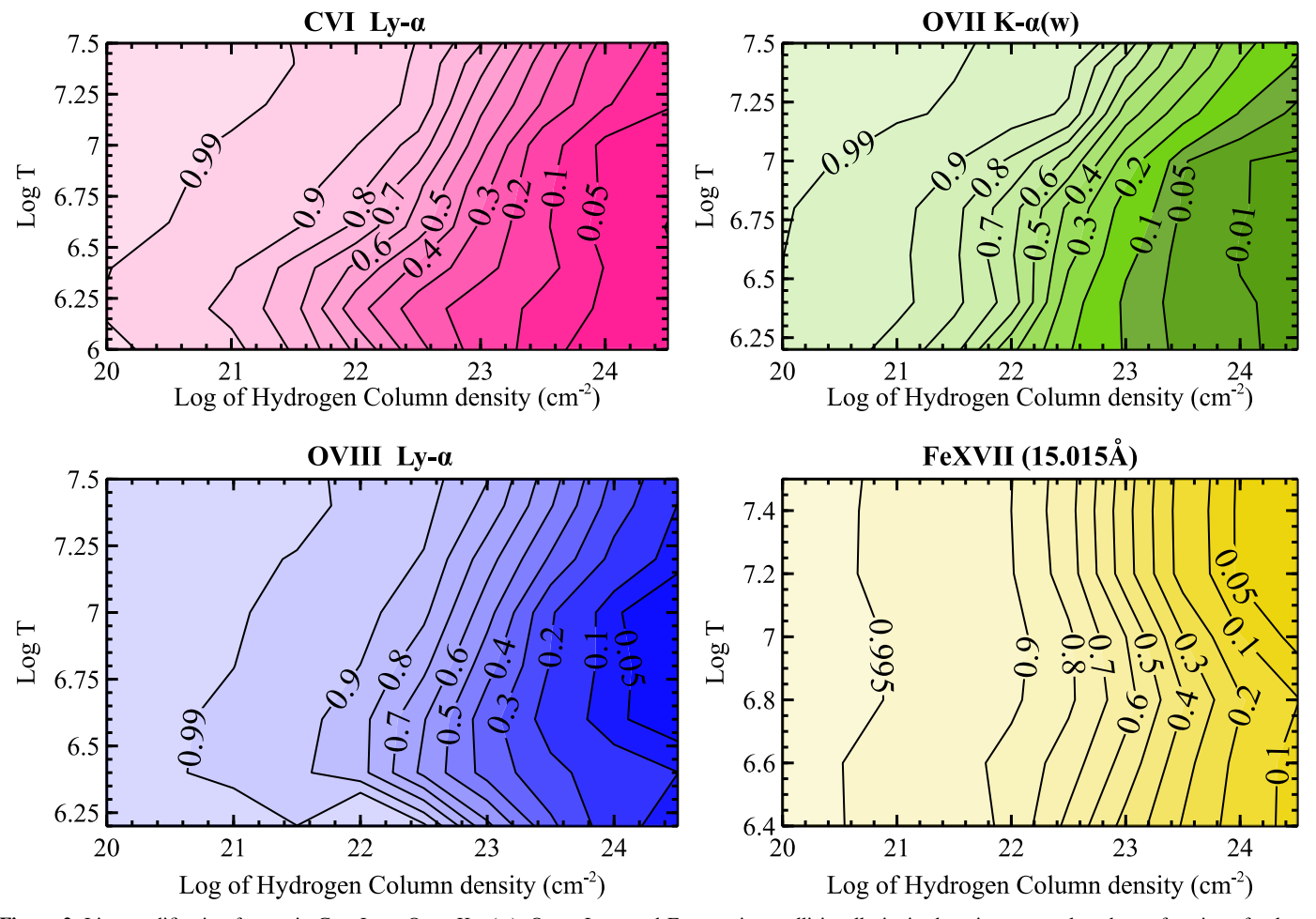


Figure 2. Line modification factors in C VI Ly α , O VII K α (w), O VIII Ly α , and Fe XVII, in a collisionally ionized environment, plotted as a function of column density and temperature.

Lyman-like lines going to the ground state⁸ are enhanced by induced radiative excitation of the atoms/ions by continuum photons in the SED. (b) Photoelectric absorption and electron scattering in line photons can suppress the line intensities.

The line ratio to be studied here is the scaled ratio of a realistic photoionized model that includes all the optical depth effects and continuum pumping, and a simplistic model excluding optical depth effects and continuum pumping.

Section 4.1 listed the CLOUDY commands for switching on/off scattering and absorption processes. The continuum pumping in the simplistic model was switched off using the CLOUDY command

no induced processes.

This ratio between the realistic and simplistic model can be smaller or larger than 1 depending on whether the suppression due to optical thickness or the enhancement due to continuum pumping is dominating. Therefore, $f_{\rm mod}$ can be smaller or larger than 1, unlike the collisionally ionized case, where $f_{\rm mod}$ can only be smaller than 1.

As mentioned in Section 3, we assumed a power-law SED with $\alpha = -1$ for demonstration. Like the previous subsection, we adopt a solar metallicity. However, α has been considered a

free parameter in Section 5 along with variable metallicity to fit the HETG spectrum of V1223 Sgr. Logs of hydrogen column density and ionization parameter have been varied to make contour plots in Figure 3.

Four contour plots in the figure show the numerical modification factor for O VII K α resonance (w) line (21.602 Å), O VIII Ly α (18.969 Å), Ne IX K α resonance (w) line (13.447 Å), and Ne X Ly α (12.134 Å). The modification factor can be as large as ~20 (enhanced about 20 times), or as small as ~0.01 (suppressed about 100 times) for the O VII K α (w) line depending on the values of $N_{\rm H}$ and ξ . The O VIII Ly α and Ne IX K α emission lines can be enhanced ~10 times, and suppressed ~100 times. The Ne X Ly α line can be enhanced ~4 times, and suppressed ~100 times. The line modification factor for important soft X-ray lines emitted from a photoionized cloud is listed in Tables 3 and 4 for $N_{\rm H} = 10^{21} \, {\rm cm}^{-2}$, $N_{\rm H} = 10^{22} \, {\rm cm}^{-2}$, and $N_{\rm H} = 10^{23} \, {\rm cm}^{-2}$ for log $\xi = 1$ and 2.5. The $f_{\rm mod}$ values for the full parameter space shown in Figure 3 can be estimated using the CLOUDY command

save line intensity,

along with previously listed CLOUDY commands in this section.

5. Application on V1223 Sgr

This section shows the application of the theory discussed in Sections 2, 3, and 4 with a slightly modified approach to

⁸ Originally Baker et al. (1938) discussed the enhancement in the line emission from atomic hydrogen. Here we have studied emissions from both H- and He-like ions. All the Lyman resonance lines become significantly enhanced, forbidden lines are slightly enhanced.

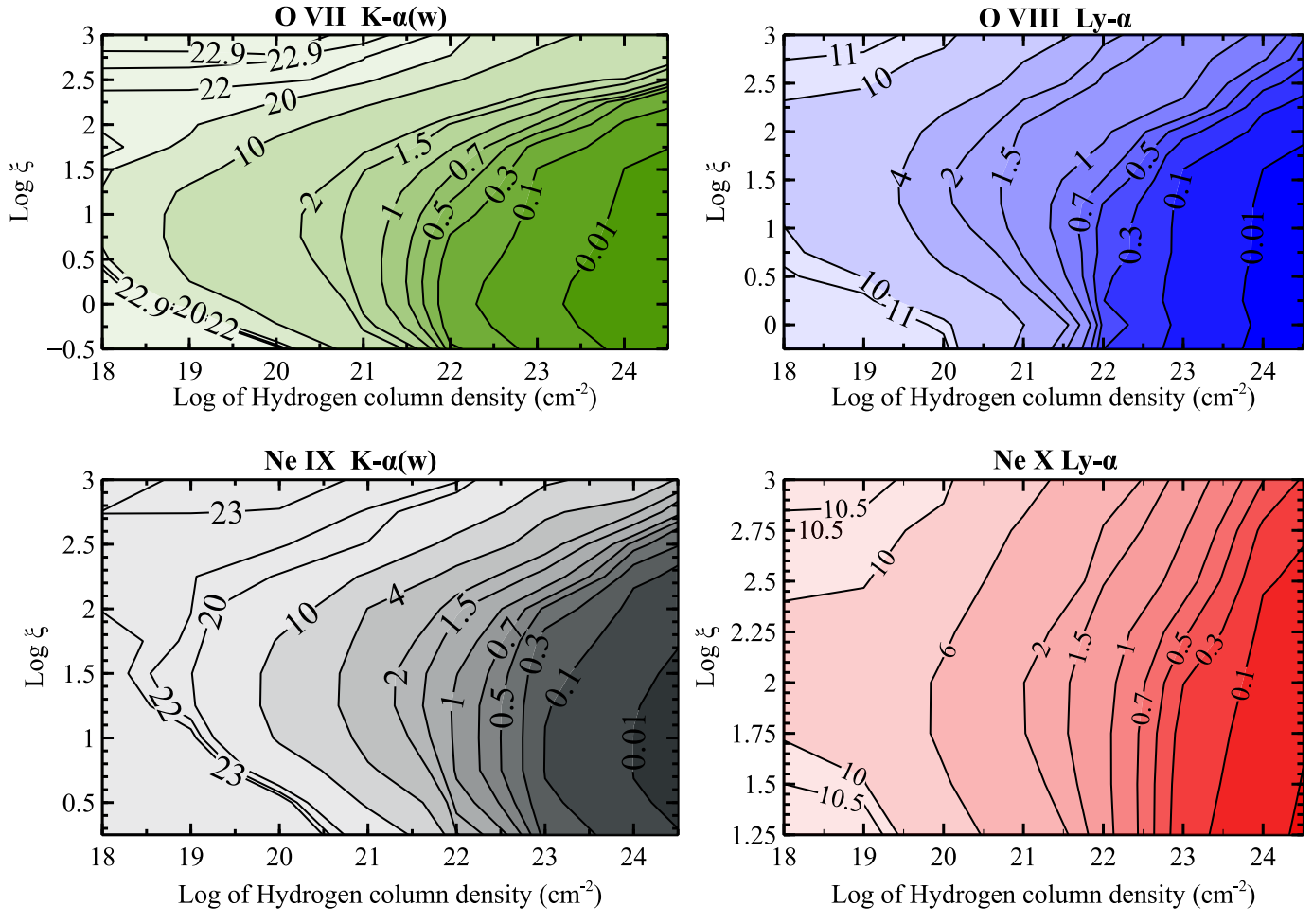


Figure 3. Line modification factor in O VII K α (w), O VIII Ly α , Ne IX K α (w), and Ne X Ly α , as a function of column density and ionization parameter (ξ).

Table 3
Line Modification Factor ($f_{\rm mod}$) in a Photoionized Cloud at $N_{\rm H}=10^{21}~{\rm cm}^{-2}, N_{\rm H}=10^{22}~{\rm cm}^{-2}$, and $N_{\rm H}=10^{23}~{\rm cm}^{-2}$ for log $\xi=1$ for Important Lines in Soft X-Ray Spectra

Transitions				$f_{ m mod}$		
	λ (Å)	Label	$N_{\rm H} = 10^{21} {\rm cm}^{-2}$	$N_{\rm H} = 10^{22} {\rm cm}^{-2}$	$N_{\rm H} = 10^{23} \rm cm^{-2}$	
C VI	33.736	Lyα	1.05	0.38	0.03	
N VI	29.082	$K\alpha(x)$	1.10	0.99	0.13	
N VI	28.787	$K\alpha$ (w)	1.75	0.72	0.07	
N VII	24.781	$Ly\alpha$	1.51	0.63	0.06	
O VII	22.101	$K\alpha$ (z)	1.08	0.87	0.11	
O VII	21.807	$K\alpha$ (y)	1.05	0.67	0.07	
O VII	21.804	$K\alpha(x)$	1.07	0.68	0.07	
O VII	21.602	$K\alpha$ (w)	1.29	0.53	0.08	
O VIII	18.969	$Ly\alpha$	1.45	0.61	0.09	
Ne IX	13.699	K α (z)	1.15	0.72	0.08	
Ne IX	13.553	K α (y)	1.16	0.73	0.08	
Ne IX	13.550	$K\alpha(x)$	1.15	0.67	0.07	
Ne IX	13.447	$K\alpha$ (w)	3.55	0.94	0.10	
Ne x	12.134	$Ly\alpha$	5.20	1.28	0.13	
Mg XI	9.314	Κ α (z)	1.25	0.65	0.07	
Mg XI	9.231	K α (y)	1.30	0.66	0.07	
Mg XI	9.228	$K\alpha(x)$	1.25	0.65	0.07	
Mg XI	9.169	$K\alpha$ (w)	18.84	4.24	0.43	
Mg XII	8.421	$Ly\alpha$	10.96	4.69	0.50	
Si XIII	6.740	Κ α (z)	1.39	0.56	0.05	
Si XIII	6.688	$K\alpha$ (y)	1.49	0.60	0.06	
Si XIII	6.685	$K\alpha(x)$	1.37	0.55	0.05	
Si XIII	6.648	$K\alpha$ (w)	31.60	12.11	1.21	

Table 4
Line Modification Factor (f_{mod}) in a Photoionized Cloud at $N_{\text{H}} = 10^{21}$ cm⁻², $N_{\text{H}} = 10^{22}$ cm⁻², and $N_{\text{H}} = 10^{23}$ cm⁻² for log $\xi = 2.5$ for Important Lines in Soft X-Ray Spectra

Transitions					
	λ (Å)	Label	$N_{\rm H} = 10^{21} {\rm cm}^{-2}$	$N_{\rm H} = 10^{22} {\rm cm}^{-2}$	$N_{\rm H} = 10^{23} {\rm cm}^{-2}$
C VI	33.736	$Ly\alpha$	7.27	2.43	1.27
N VI	29.082	$K\alpha(x)$	0.99	0.96	0.95
N VI	28.787	$K\alpha$ (w)	23.74	21.32	13.37
N VII	24.781	$Ly\alpha$	7.86	2.73	1.24
O VII	22.101	$K\alpha$ (z)	0.99	0.96	0.90
O VII	21.807	$K\alpha$ (y)	1.0	0.98	0.91
O VII	21.804	$K\alpha(x)$	0.99	0.97	0.91
O VII	21.602	$K\alpha$ (w)	22.06	11.12	6.74
O VIII	18.969	$Ly\alpha$	3.65	1.59	1.39
Ne IX	13.699	Κ α (z)	1.26	1.03	1.01
Ne IX	13.553	$K\alpha$ (y)	1.29	1.04	1.02
Ne IX	13.550	$K\alpha(x)$	1.27	1.03	1.01
Ne IX	13.447	$K\alpha$ (w)	19.85	11.88	4.33
Ne X	12.134	$Ly\alpha$	3.55	2.60	2.31
Mg XI	9.314	$K\alpha$ (z)	1.16	1.04	1.03
Mg XI	9.231	$K\alpha$ (y)	1.20	1.08	1.07
Mg XI	9.228	$K\alpha(x)$	1.16	1.04	1.03
Mg XI	9.169	$K\alpha$ (w)	16.75	5.02	1.91
Mg XII	8.421	$Ly\alpha$	4.88	1.87	0.95
Si XIII	6.740	$K\alpha$ (z)	1.10	1.08	1.07
Si XIII	6.688	$K\alpha$ (y)	1.16	1.15	1.14
Si XIII	6.685	$K\alpha(x)$	1.09	1.08	1.06
Si XIII	6.648	$K\alpha$ (w)	11.83	3.54	1.38
Si XIV	6.182	$Ly\alpha$	5.24	2.00	0.99

treat the multiphase plasma for the collisionally ionized case (refer to Section 5.2). We show the application on the Intermediate Polar V1223 Sgr, consisting of a white dwarf (WD) accreting material from a low-mass secondary star. The matter stripped from the secondary star is magnetically channeled onto a truncated accretion disk around the white dwarf (Patterson 1994). The X-rays from Intermediate Polars are generated when the infalling high-velocity (3000–10,000 km s⁻¹⁻¹) matter encounters a shock while falling onto the white dwarf surface. The infalling particles then decelerate further in a subsonic cooling column before hitting the surface of the white dwarf. The inner flow produces strong X-ray emission.

As displayed in Figures 2 and 3, the optical depth effects are expected to modify the important lines in the soft X-ray spectra at high column densities ($N_{\rm H} \ge 10^{22.5} \, {\rm cm}^{-2}$). V1223 Sgr is an ideal candidate for applying our theory, as Islam & Mukai (2021) estimated that this Intermediate Polar has a fairly large column density ($\sim 10^{23} \, \text{cm}^{-2}$). They used a combination of a cooling-flow model (containing emission lines from multitemperature collisionally ionized plasma, and bremsstrahlung), an ionized complex absorber model, and X-ray reflection to model the summed first-order Chandra MEG spectrum of V1223 Sgr. They reported an excess flux from O VII, O VIII, Ne IX, Ne X, and Mg XI lines (see Figure 3 in their paper), which could not be described with their model, and implied that these lines could have a photoionization origin. The photoionized emission in CVs likely generates in the preshock region that is ionized by the X-ray radiation emitted in the postshock region (Luna et al. 2010). We have also fitted the same spectrum with CLOUDY and the detailed models are described in Sections 5.2 and 5.3.

Table 5
Archival Chandra ACIS-S/HETG Observation of V1223 Sgr

Observation ID	Start Date/Time	Exposure (ks)
649	2000-04-30/16:19:51	51.48

5.1. Data Reduction

We redo the Chandra/HETG data analysis of V1223 Sgr, previously done by Islam & Mukai (2021). The observational log of the spectrum is listed in Table 5. We obtained the first-order MEG spectrum with the corresponding response files from the TGCat archive (Huenemoerder et al. 2011, 2013). Data processing was performed using CIAO-4.13 (Fruscione et al. 2006) and CALDB version 4.9.4. All first-order spectra and associated responses for MEG were combined using the CIAO tool combine_spectra. The combined spectrum was grouped using the CIAO tool dmgroup with at least 30 counts per bin. This particular lower limit has been set to maintain sufficient counts for the spectral fitting while preserving the resolution of the spectra. Black data points in Figure 4 represent the final spectrum.

5.2. Modeling Multiphase Plasma with Cooling-flow CLOUDY Simulation

The atomic physics and the line modification factor described for collisionally ionized plasma in Section 4.1 was done for a single-temperature static model for the purpose of demonstration. V1223 Sgr is a multiphase system, which requires the consideration of the evolution of plasma cooling with time. Chatzikos et al. (2015) used CLOUDY to compute the spectrum of a unit volume of gas in collisional ionization

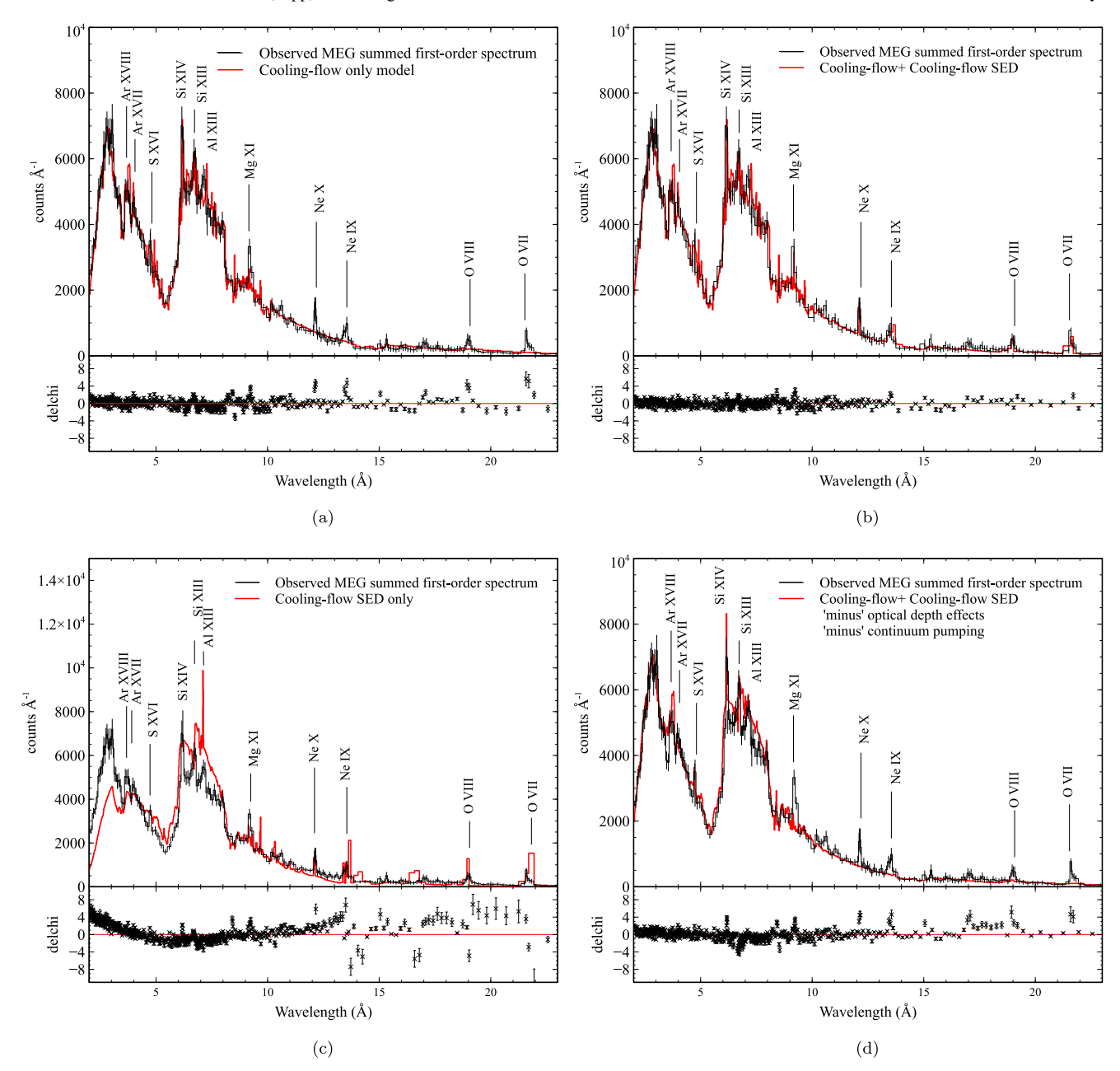


Figure 4. On all four panels, black data points show the Chandra High-Energy Transmission Grating MEG combined first-order spectrum. (a) The solid red line shows our best-fit cooling-flow SED CLOUDY model. (b) The solid red line shows the best-fit cooling-flow + cooling-flow SED CLOUDY model. (c) The solid red line shows the cooling-flow SED only CLOUDY model. (d) The solid red line shows our best-fit cooling-flow + cooling-flow SED CLOUDY model without considering the optical depth and continuum pumping effects discussed in Sections 2, 3, and 4.

equilibrium cooling from $\sim 10^8$ to 10^4 K. We adopt a similar approach with a finite volume of gas and variable column density. The cooling-flow model used in our CLOUDY simulation consists of a multiphase plasma that cools from 4×10^8 K. The upper limit in temperature has been set following the previous studies with Intermediate Polars (Anzolin et al. 2008; Islam & Mukai 2021). We attempted to let the gas cool down to 10^4 K, but the solution was numerically unstable below 2×10^6 K, so we presented the result down to that temperature. The impact of neglecting the emission below 2×10^6 K has been discussed in Section 5.3. The observed spectrum was well fitted by the cooling-flow model except for the emission from O VII, O VIII, Ne IX, Ne X, and Mg XI, which is in agreement with Islam & Mukai (2021).

We attempted to fit the excess emission from these lines with a photoionized model using the diffuse emission from the cooling flow as the SED to photoionize the gas in the preshock region. The cooling-flow SED was extracted with the CLOUDY command save continuum. The following subsection further describes the parameters and grids employed in our cooling-flow simulation.

5.3. CLOUDY Models Fitting the Observed Spectrum

We fit the observed spectrum with the following: (a) pure cooling-flow model; (b) cooling-flow + photoionized model; (c) pure photoionized model; and (d) cooling-flow + photoionized model without considering the optical depth and continuum pumping effects discussed in Sections 2, 3, and 4.

Table 6

Best-fit Parameters for (a) Cooling-flow Only, (b) Cooling-flow + Cooling-flow SED, (c) Cooling-flow SED Only, and (d) Cooling-flow + Cooling-flow SED Model Excluding Continuum Pumping and Optical Depth Effects Fitting the Summed First-order MEG Spectrum of V1223 Sgr

	Best-fit Values			
Parameter	(a)	(b)	(c)	(d)
$\log \xi$	•••	$1.664_{-0.007}^{+0.009}$	$0.853^{+0.003}_{-0.004}$	$1.612^{+0.006}_{-0.005}$
$\log N_{\mathrm{H}_{photo}}$	•••	$22.93 ^{ +0.03}_{ -0.04}$	$22.93^{+0.04}_{-0.03}$	$23.39_{-0.03}^{+0.03}$
$N_{\rm photo} \ (\times 10^{-24} \ {\rm ph \ keV^{-1} \ cm^{-2}})$	•••	$0.46^{+0.04}_{-0.04}$	$6.51^{+0.02}_{-0.01}$	$0.25^{+0.03}_{-0.04}$
Metallicity	0.40 ± 0.03	0.40 ± 0.04	0.44 ± 0.03	0.45 ± 0.03
$N_{\rm coll} \ (\times 10^{-24} \ \rm ph \ keV^{-1} \ cm^{-2})$	$4.86^{+0.30}_{-0.20}$	$2.23^{+0.41}_{-0.41}$		$6.34^{+0.32}_{-0.20}$
$\log N_{ m H_{coll}}$	$23.13 \begin{array}{l} +0.03 \\ -0.02 \end{array}$	$23.11 ^{+0.05}_{-0.04}$		$23.08^{+0.03}_{-0.04}$
χ^2	876.80/629	639.63/626	3233.08/628	988.35/626

The source of photoionizing radiation in the last three models is the diffuse radiation emitted by the cooling-flow plasma. The CLOUDY commands to switch off optical depth effects and continuum pumping are

no absorption escape, no induced processes.

We use the CLOUDY/XSPEC interface (Porter et al. 2006) to import the models into XSPEC (Arnaud 1996). Galactic absorption was included using the XSPEC routine tbabs, with the absorbing hydrogen column density set to $0.09 \times 10^{21} \, \mathrm{cm}^{-2}$ toward V1223 Sgr. The complete models as imported to XSPEC are (a) tbabs atable (cooling-flow.fits), (b) tbabs (atable (cooling-flow.fits) + atable (photoionized.fits)), (c) tbabs atable (photoionized.fits), and (d) tbabs (atable (cooling-flow.fits)) enabling CLOUDY commands stated in the previous paragraph.

A chi-square statistics was used to fit the spectrum. This is a straightforward approach for fitting the spectrum while considering all the atomic processes happening in the cloud, including absorption and scattering. The cooling-flow model has grids on log of column density ($N_{\rm H_{coll}}$), and metallicity. The photoionized model has grids on the log of column density ($N_{\rm H_{photo}}$), log of ionization parameter (ξ), and metallicity. For (b) and (d), we tie the metallicity of the cooling-flow and photoionized models, and let $\log N_{\rm H_{coll}}$, $\log N_{\rm H_{photo}}$, $\log \xi$, and normalization of the models ($N_{\rm photo}$, $N_{\rm coll}$) vary freely. A solar abundance table by Asplund et al. (2009) was used for all our calculations. An electron density of $10^{14} \, {\rm cm}^{-3}$ was assumed (Beuermann et al. 2004; Kuulkers et al. 2006). The sample CLOUDY scripts used for generating the XSPEC compatible. fits files are given in Appendix A.

Note that spectral signatures of X-ray reflection from the surface of the WD have been discussed in a number of studies (Beardmore et al. 1995; Cropper et al. 1998; Beardmore et al. 2000; Hayashi et al. 2011; Mukai et al. 2015; Islam & Mukai 2021; Hayashi et al. 2021). X-ray reflection primarily produce two distinctive features: a Compton reflection hump at \sim 10–30 keV, and iron fluorescent K α line at 6.4 keV. CLOUDY

simulations include these features by default. The MEG spectrum covers the energy range 0.4–5.0 keV (31–2.5 Å), where there are fluorescence lines from lighter elements. In the case of V1223 Sgr, they are much fainter than the iron fluorescence line, and thus negligible. This is not always true. For example, emission spectrum from the High Mass X-ray Binary Vela X–1 exhibits fluorescent Si and S K α lines (Amato et al. 2021; Camilloni et al. 2021).

The complete CLOUDY models have been overplotted with the observed spectrum in Figure 4. The red line represents our best-fit CLOUDY model, and the black data points represent the observed spectrum. The top-left, top-right, bottom-left, and bottom-right panels show the best-fit CLOUDY models using cooling-flow only, cooling-flow + photoionized, photoionized only, and cooling-flow + photoionized without considering the optical depth and continuum pumping.

- (a) The cooling-flow only model fits the continuum well and contributes to the formation of Al XIII, Si XIII, Si XIV, S XVI, Ar XVII, and Ar XVIII lines. O VII, O VIII, Ne IX, Ne X, and Mg XI lines could not be fit with the cooling-flow model, which favors the findings of Islam & Mukai (2021).
- (b) The cooling-flow + photoionized model produces a significantly better fit for O VII, O VIII, Ne IX, Ne X, and Mg XI lines than the cooling-flow only model. The ionization fraction for ${\rm O^{7+}}$, Ne⁸⁺, Ne⁹⁺, and Mg I⁰⁺ peaks at temperatures greater than 2×10^6 K, where we artificially stopped the cooling-flow CLOUDY model. It is, therefore safe to infer that emission from O VIII, Ne IX, Ne X, and Mg XI lines mostly comes from photoionization. As the ionization fraction for ${\rm O^{6+}}$ peaks at $\sim 8\times 10^5$ K, we could not check if the cooling-flow model contributes to the O VII line emission and to what extent. Future papers will address the numerical instability issue of the cooling-flow model at lower temperatures.
- (c) The pure photoionized model produces a poor fit to the spectrum in the lower wavelength region with missing Si XIII, Si XIV, S XVI, Ar XVII, and Ar XVIII lines.
- (d) The cooling-flow + photoionized model with the optical depth effects and continuum pumping switched off produces a considerably worse fit to the observed spectrum than that including these atomic processes, especially the fit to the continuum and emission lines from O VII, O VIII, Ne IX, Ne X, Mg XI, and Si XIV. This shows the importance of taking into account the effects of optical depth and continuum excitation.

Table 6 lists CLOUDY model parameters fitting the observed spectrum for (a), (b), (c), and (d) at a 90% confidence interval. The best fit is obtained for model (b), with all the other fits being substantially worse.

https://heasarc.gsfc.nasa.gov/cgi-bin/Tools/w3nh/w3nh.pl

¹⁰ Homer et al. (2004) showed that line intensities/ratios remain the same in the Intermediate Polar V426 Oph, regardless of the isochoric/isobaric nature of the cooling flow. Revaz & Jablonka (2012) also used an isochoric cooling-flow model for modeling plasma with temperatures hotter than 10⁴ K. In addition, part of the geometry in IPs is controlled by moderate magnetic fields (Gális et al. 2011). An isochoric cooling-flow CLOUDY model was, therefore, the simplest assumption for the application on V1223 Sgr.

6. Summary

- 1. The effects of optical depth have been discussed on soft X-ray emission lines. A cloud can be collisionally ionized or photoionized. For a collisionally ionized cloud, the atomic physical processes that contribute to the suppression in soft X-ray lines are photoelectric absorption of line photons and electron scattering. Photoelectric absorption is temperature dependent; electron scattering is not. The temperature dependence of photoelectric absorption opacity is shown on Figure 1. The line modification factor (f_{mod}) quantifies the fraction of photons surviving the absorption and scattering (see Equation (1)). Figure 2 shows the numerical equivalent of $f_{\rm mod}$ as a function of hydrogen column density and temperature for C VI Ly α , O VII K α (w), O VIII Ly α , and Fe XVII lines. Tables 1 and 2 list $f_{\rm mod}$ for important soft X-ray lines at $N_{\rm H}=10^{22}\,{\rm cm}^{-2}$, $N_{\rm H}=10^{22.5}\,{\rm cm}^{-2}$, and $N_{\rm H}=10^{23}\,{\rm cm}^{-2}$ and log T=6.4 and 6.8. For a collisionally ionized cloud, $0 \le f_{\text{mod}} \le 1$. As shown in the tables, f_{mod} is smaller for lower-Z elements like carbon, oxygen, and neon, but approaches 1 for higher-Z elements like magnesium, silicon, and sulfur. This implies that soft X-ray line intensities for the lower-Z elements can be significantly suppressed.
- 2. For the photoionized cloud, lines can be enhanced or suppressed. Continuum pumping can strengthen the Lyman lines in H- and He-like ions. Absorption and scattering can suppress the lines. Whether a line will be suppressed or enhanced is jointly determined by these two factors. Unlike the collisionally ionized cloud, $f_{\rm mod}$ can be greater or smaller than 1. Figure 3 shows the numerical equivalent of $f_{\rm mod}$ as a function of hydrogen column density and ionization parameter for an $\alpha=-1$ power-law SED for O VII K α (w), O VIII Ly α , Ne IX K α (w), and Ne X Ly α . Tables 3 and 4 show $f_{\rm mod}$ for important soft X-ray photoionized lines for $N_{\rm H}=10^{21}\,{\rm cm}^{-2}$, $N_{\rm H}=10^{22}\,{\rm cm}^{-2}$, and $N_{\rm H}=10^{23}\,{\rm cm}^{-2}$ for log $\xi=1$, and 2.5.
- 3. A hybrid of collisional ionization and photoionization is also observed in many astronomical sources. One such example is illustrated in Section 5. We modeled the MEG spectrum from V1223 Sgr, an Intermediate Polar, using the CLOUDY/XSPEC interface. This is the first application of this interface after the recent CLOUDY developments for meeting the spectroscopic standards of the future microcalorimeter missions. We used a combination of CLOUDYsimulated cooling-flow (collisionally ionized plasma cooling from 4×10^8 K to 2×10^6 K) and photoionized models to fit the spectrum. The photoionized model represents the emission from gas in the preshock region that has been ionized by the diffuse emission from the cooling-flow plasma. The lower limit in temperature for the cooling-flow model was set to be 2×10^6 K to avoid the numerical instability issues as described in Section 5.2. We found that the cooling-flow model dominates the shape of the continuum. Emissions from Al XIII, Si XIII, Si XIV, S XVI, Ar XVII, and Ar XVIII lines originate in the cooling-flow plasma. O VII, O VIII, Ne IX, Ne X, and Mg XI lines originate in the photoionized plasma. Islam & Mukai (2021) fitted the same spectrum of V1223 Sgr and reported excess emission from O VII, O VIII, Ne IX, Ne X, and Mg XI lines, which could not be described with their absorbed cooling-flow model. We fit these lines simply by adding the

photoionized component to the standard cooling-flow component. Table 6 lists the best-fit parameters from our best-fit CLOUDY model. The top-right panel of Figure 4 shows the best-fit CLOUDY model overplotted with the observed spectrum. On the contrary, the observed spectrum was ill-fitted using pure cooling-flow and pure photoionized CLOUDY models, as shown in the top-left and bottom-left panels of Figure 4. We also show the consequences of switching off atomic physical processes like optical depth effects and continuum pumping in the bottom-right panel of the figure. The solid red line shows the fit after switching off the atomic physical processes. The fit is considerably worse than our best-fit model shown on the top-right panel, including all atomic processes. This shows the importance of incorporating optical depth effects and continuum pumping in the spectral simulation codes.

We acknowledge support by NSF (1816537, 1910687), NASA (17-ATP17-0141, 19-ATP19-0188), and STScI (HST-AR-15018). M.C. also acknowledges support from STScI (HST-AR-14556.001-A). S.B. acknowledges financial support from the Italian Space Agency (grant 2017-12-H.0) and from the PRIN MIUR project black hole winds and the BaryonLife Cycle of Galaxies: the stone-guest at the galaxy evolution supper, contract 2017-PH3WAT.

Appendix A

CLOUDY script for generating XSPEC compatible coolingflow model spectrum (where T_1 and T_2 are input parameters for temperature):

```
coronal T_1 K init time # Plasma starts cooling from T_1 K
hden 13.92
no scattering intensity
stop column density 20 vary
grid 20 24 0.5
metal solar -1 log vary
grid -1 0 0.2
abundances GASS10
iterate 3000
no molecules
stop time when temperature falls below T_2 K \# Plasma stops
 cooling at T_2 K
stop temperature T2 K
save xspec atable total continuum 'cooling-flow.fits''
CLOUDY script for generating XSPEC compatible photoionized model
table sed 'cool.sed''
xi - 1 vary
grid 0.5 2.5 0.5
hden 13.92
no scattering intensity
stop column density 20 vary
grid 20 24 0.5
metal solar -1 log vary
grid -1 0 0.2
abundances GASS10
save xspec atable total continuum 'photoionized.fits''
```

Appendix B

Before version 17.03, CLOUDY used the Chianti atomic database (Dere et al. 1997; Landi et al. 2012) as described in

Lykins et al. (2015) for Fe¹⁶⁺ energy levels. With 17.03, we updated the masterlist to use the first 30 levels for Fe¹⁶⁺ from the NIST atomic database (Kramida et al. 2018) by default, which improved the wavelength for the Fe XVII $3C^{\dagger}$ transition from 15.0130 to 15.0150 Å.

ORCID iDs

Priyanka Chakraborty https://orcid.org/0000-0002-

```
4469-2518
Gary J. Ferland https://orcid.org/0000-0003-4503-6333
Marios Chatzikos https://orcid.org/0000-0002-8823-0606
Andrew C. Fabian https://orcid.org/0000-0002-9378-4072
Stefano Bianchi https://orcid.org/0000-0002-4622-4240
Francisco Guzmán https://orcid.org/0000-0002-2915-3612
Yuanyuan Su https://orcid.org/0000-0002-3886-1258
```

```
References
Amato, R., Grinberg, V., Hell, N., et al. 2021, A&A, 648, A105
Anzolin, G., de Martino, D., Bonnet-Bidaud, J. M., et al. 2008, A&A,
  489, 1243
Arnaud, K. A. 1996, in ASP Conf. Ser., 101, Astronomical Data Analysis
   Software and Systems V, ed. G. H. Jacoby & J. Barnes (San Francisco, CA:
Asplund, M., Grevesse, N., Sauval, A. J., & Scott, P. 2009, ARA&A, 47, 481
Baker, J. G., & Menzel, D. H. 1938, ApJ, 88, 52
Baker, J. G., Menzel, D. H., & Aller, L. H. 1938, ApJ, 88, 422
Band, D. L., Klein, R. I., Castor, J. I., & Nash, J. K. 1990, ApJ, 362, 90
Beardmore, A. P., Done, C., Osborne, J. P., & Ishida, M. 1995, MNRAS,
Beardmore, A. P., Osborne, J. P., & Hellier, C. 2000, MNRAS, 315, 307
Beuermann, K., Harrison, T. E., McArthur, B. E., Benedict, G. F., &
   Gänsicke, B. T. 2004, A&A, 419, 291
Brown, G. V., Beiersdorfer, P., Liedahl, D. A., Widmann, K., & Kahn, S. M.
  1998, ApJ, 502, 1015
Camilloni, F., Bianchi, S., Amato, R., Ferland, G., & Grinberg, V. 2021,
Chakraborty, P., Ferland, G. J., Chatzikos, M., Guzmán, F., & Su, Y. 2020a,
   ApJ, 901, 68
Chakraborty, P., Ferland, G. J., Chatzikos, M., Guzmán, F., & Su, Y. 2020b,
   ApJ, 901, 69
Chakraborty, P., Ferland, G. J., Chatzikos, M., Guzmán, F., & Su, Y. 2021,
   ApJ, 912, 26
Chamberlain, J. W. 1953, ApJ, 117, 399
Chatzikos, M., Williams, R. J. R., Ferland, G. J., et al. 2015, MNRAS,
   446, 1234
```

```
Cropper, M., Ramsay, G., & Wu, K. 1998, MNRAS, 293, 222
de Plaa, J., Zhuravleva, I., Werner, N., et al. 2012, A&A, 539, A34
Dere, K. P., Landi, E., Mason, H. E., Monsignori Fossi, B. C., & Young, P. R.
  1997, A&AS, 125, 149
Ferland, G., & Netzer, H. 1979, ApJ, 229, 274
Ferland, G. J. 1999, PASP, 111, 1524
Ferland, G. J., Chatzikos, M., Guzmán, F., et al. 2017, RMxAA, 53, 385
Fruscione, A., McDowell, J. C., Allen, G. E., et al. 2006, Proc. SPIE, 6270,
Gális, R., Hric, L., Kundra, E., & Münz, F. 2011, AcPol, 51, 13
Hayashi, T., Ishida, M., Terada, Y., Bamba, A., & Shionome, T. 2011, PASJ,
  63. S739
Hayashi, T., Kitaguchi, T., & Ishida, M. 2021, MNRAS, 504, 3651
Homer, L., Szkody, P., Raymond, J. C., et al. 2004, ApJ, 610, 991
Huenemoerder, D., Nowak, M., Dewey, D., Schulz, N., & Mitschang, A. 2013,
  TGCat: Chandra Transmission Grating Catalog and Archive, Astrophysics
  Source Code Library, ascl:1303.012
Huenemoerder, D. P., Mitschang, A., Dewey, D., et al. 2011, AJ, 141, 129
Hummer, D. G., & Storey, P. J. 1992, MNRAS, 254, 277
Islam, N., & Mukai, K. 2021, ApJ, 919, 90
Kramida, A., Ralchenko, Y., Nave, G., & Reader, J. 2018, APS Division of
   Atomic, Molecular and Optical Physics Meeting Abstracts (College Park,
  MD: APS), M01.004
Kuulkers, E., Norton, A., Schwope, A., & Warner, B. 2006, Compact Stellar
  X-ray Sources, Vol. 39 (Cambridge: Cambridge Univ. Press), 421
Landi, E., Del Zanna, G., Young, P. R., Dere, K. P., & Mason, H. E. 2012,
   ApJ, 744, 99
Liedahl, D. A. 2005, in AIP Conf. Ser., 774, X-ray Diagnostics of
  Astrophysical Plasmas: Theory, Experiment, and Observation, ed.
  R. Smith (Melville, NY: AIP), 99
Luna, G. J. M., Raymond, J. C., Brickhouse, N. S., et al. 2010, ApJ, 711, 1333
Luridiana, V., Simón-Díaz, S., Cerviño, M., et al. 2009, ApJ, 691, 1712
Lykins, M. L., Ferland, G. J., Kisielius, R., et al. 2015, ApJ, 807, 118
Matzeu, G. A., Nardini, E., Parker, M. L., et al. 2020, MNRAS, 497, 2352
Mukai, K., Rana, V., Bernardini, F., & de Martino, D. 2015, ApJL, 807,
Okada, S., Nakamura, R., & Ishida, M. 2008, ApJ, 680, 695
Patterson, J. 1994, PASP, 106, 209
Peimbert, A., Peimbert, M., & Luridiana, V. 2016, RMxAA, 52, 419
Pintore, F., & Zampieri, L. 2011, AN, 332, 337
Porter, R. L., Ferland, G. J., Kraemer, S. B., et al. 2006, PASP, 118, 920
Ramsay, G., & Cropper, M. 2002, MNRAS, 334, 805
Rauch, T., Werner, K., & Orio, M. 2005, in AIP Conf. Ser., 774, X-ray
  Diagnostics of Astrophysical Plasmas: Theory, Experiment, and
  Observation, ed. R. Smith (San Francisco, CA: ASP), 361
Rees, M. J., Netzer, H., & Ferland, G. J. 1989, ApJ, 347, 640
Revaz, Y., & Jablonka, P. 2012, A&A, 538, A82
Ross, R. R., Fabian, A. C., & Brandt, W. N. 1996, MNRAS, 278, 1082
Ross, R. R., Weaver, R., & McCray, R. 1978, ApJ, 219, 292
Storey, P. J., & Hummer, D. G. 1988, MNRAS, 231, 1139
```